Available online at www.sciencedirect.com

ScienceDirect

Journal of Magnesium and Alloys 9 (2021) 1806–1819

www.elsevier.com/locate/jma

On the evaluation of ALD TiO_2, ZrO_2 and HfO_2 coatings on corrosion and cytotoxicity performances

Mirco Peron[a,*], Susanna Cogo[b], Maria Bjelland[a], Abdulla Bin Afif[a], Anup Dadlani[a], Elisa Greggio[b], Filippo Berto[a], Jan Torgersen[a]

[a] *Department of Industrial and Mechanical Engineering, Norwegian University of Science and Technology, Richard Birkelands vei 2b, 7034 Trondheim, Norway*

[b] *Department of Biology, University of Padova, Via Ugo Bassi 58/b, 35131, Padova, Italy*

Received 20 October 2020; received in revised form 28 February 2021; accepted 13 March 2021
Available online 15 May 2021

Abstract

Magnesium alloys have been widely studied as materials for temporary implants, but their use has been limited by their corrosion rate. Recently, coatings have been proven to provide an effective barrier. Though only little explored in the field, Atomic Layer Deposition (ALD) stands out as a coating technology due to the outstanding film conformality and density achievable. Here, we provide first insights into the corrosion behavior and the induced biological response of 100 nm thick ALD TiO_2, HfO_2 and ZrO_2 coatings on AZ31 alloy by means of potentiodynamic polarization curves, electrochemical impedance spectroscopy (EIS), hydrogen evolution and MTS colorimetric assay with L929 cells. All three coatings improve the corrosion behavior and cytotoxicity of the alloy. Particularly, HfO_2 coatings were characterized by the highest corrosion resistance and cell viability, slightly higher than those of ZrO_2 coatings. TiO_2 was characterized by the lowest corrosion improvements and, though generally considered a biocompatible coating, was found to not meet the demands for cellular applications (it was characterized by grade 3 cytotoxicity after 5 days of culture). These results reveal a strong link between biocompatibility and corrosion resistance and entail the need of taking the latter into consideration in the choice of a biocompatible coating to protect degradable Mg-based alloys.

Keywords: Atomic layer deposition (ALD); Coatings; Corrosion resistance; Cytocompatibility; Magnesium.

1. Introduction

As aging and obesity increase the demand for the implantation of medical devices [1], medical technology advances, with a raising interest in the use of metallic materials for implantable devices to assist with tissue repair or replacement. Implantable devices can be divided into permanent and temporary. For the latter, implants are only required to remain within the human body until the tissue regains load bearing capacity and integrity. To this aim, biodegradable materials are desired and Magnesium (Mg) stands out [2–4] due to its attractive features: (1) an elastic modulus compatible with natural bone minimizing the risk of stress shielding [2] and (2) the ability to degrade in vivo without releasing toxic products [5–7]. Accelerated corrosion of pure Mg hampers its usability in clinical applications as mechanical failure of the implant is prone to occur before the tissue has recovered [8]. In addition, during corrosion, hydrogen gas gets produced at rates beyond what bone tissue is able to accommodate, causing severe host tissue damage [9,10].

In the last years, different strategies have been investigated to reduce the corrosion rate of Mg, such as alloying and mechanical processing inducing severe plastic deformation (SPD) like Equal Channel Angular Pressing (ECAP) and machining [11–14]. However, both these approaches are char-

* Corresponding author.
E-mail address: mirco.peron@ntnu.no (M. Peron).

https://doi.org/10.1016/j.jma.2021.03.010

acterized by some main limitations. Alloying may introduce elements causing adverse biological reactions [15], ECAP requires multiple deformation passes before achieving the goal, while machining might not be applicable in the development of Mg implants as it does not allow to make the intricate features and textured surfaces needed to enhance ingrowth of cells and tissue [16–18].

Hence, an alternative, surface confined approach allowing the control of surface texture might be required. In this perspective, coatings have recently gained wide interest among researchers since they allow to preserve the surface texture and the designed macroscopic porosity tailored for osseointegration and to match mechanical characteristics. Several coating techniques, such as anodizing, fluoride conversion coating, sol-gel techniques and physical vapor deposition techniques, have been developed in the last years to increase the corrosion resistance [19]. However, all these techniques are characterized by some drawbacks that limit their use, mainly low control of the thickness and high porosity and cracking [20–22]. In addition, the effectiveness of physical vapor deposition techniques, such as sputtering, may be limited due to the inherent line-of-sight deposition process [23,24].

To overcome this issue, Chemical Vapor Deposition (CVD) is employed. In this class of processes, the substrate surface is exposed to one or more volatile precursors that react and/or decompose to produce the desired surface deposit. Among CVD techniques, Atomic Layer Deposition (ALD) stands out in terms of conformality, film density and possibility for compositional control due to its self-limiting surface-gas phase reactions and it has recently found application in corrosion protection of biomedical implants [25,26]. In this field, researchers have mainly focused on the effect of biocompatible coatings deposited by means of ALD on the corrosion resistance of metallic implant materials [27,28]. In particular, their interest has focused on TiO_2 and ZrO_2. TiO_2 is in fact known to be biocompatible since it can (1) stimulate in vivo osteoconductivity [29–31], (2) induce in vitro bone-like apatite formation and (3) bind directly and reliably to living bone [32]. On the other hand, ZrO_2 is an important biomaterial, widely used in applications such as dental implants, where osteointegration is of minor importance compared to the requirements of corrosion and wear resistance [33] and of a reduced bacterial colonization [34,35]. Dealing with Mg and its alloys, although limited data are available, the application of both ALDed TiO_2 and ZrO_2 has been shown to promisingly improve the corrosion resistance. Marin et al. [26] reported a reduced corrosion current density (i.e., from 10^{-4} A/cm^2 to 10^{-6} A/cm^2) when a commercial AZ31 Mg alloy was coated with a 100 nm thick TiO_2 layer, while a 10 nm thick ZrO_2 layer was found to reduce the corrosion current density of an AZ31 Mg alloy by three order of magnitude [25], agreeing with the results obtained by our group for a 100 nm thick ZrO_2 layer [36–38].

However, in the development of reliable Mg-based implants, and more in general of temporary implants, the corrosion resistance of a material is fundamental also because it can affect the cell response: degradation products evolving during the corrosion process may in fact cause adverse effect on the surrounding (the vicinity of the implant). In the case of Mg and its alloys, H_2 evolves from the corrosion process. This leads to an increase in the pH around the implant, and it is widely known that a high pH has harmful effects on cell viability, migration and proliferation [39]. For example, a pH higher than 8.5 was reported to inhibit the proliferation of human bone marrow-derived mesenchymal stem cells [40]. Nevertheless, to the best of the authors' knowledge, the cytotoxicity of ALD TiO_2 and ZrO_2 coatings has never been evaluated.

In this work, we aim to evaluate the effect of TiO_2 and ZrO_2 ALD coatings on cell viability in the vicinity of the implant by carrying out MTS proliferation assay using the murine subcutaneous connective tissue L929 cell line. Moreover, to provide further insights into the corrosion performances of ALD TiO_2 and ZrO_2 coatings in a physiologically relevant environment, potentiodynamic polarization curves, electrochemical impedance spectroscopy (EIS) and hydrogen evolution tests have been carried out on 100 nm thick TiO_2 and ZrO_2 coated AZ31 samples. In addition to that, a new biocompatible coating has recently emerged as a very effective coating material to increase the corrosion resistance of biocompatible materials [41], i.e. HfO_2. Zhang et al., in fact, reported a 30 nm HfO_2 coating to reduce the corrosion current density of a die-cast AZ91D from 44.29 μA/cm^2 to 0.78 μA/cm^2 [42]. These results agree with those reported in Ref. [43] where 60 nm HfO_2 coating was reported to decrease the corrosion current density of an AZ31 alloy of almost three orders of magnitude. However, much still needs to be uncovered, since very few studies have addressed this aspect. Moreover, to the best of the authors' knowledge, the effects of ALD HfO_2 on cell viability have never been investigated before. Hence, with this work, we also aim to fill these gaps, carrying out potentiodynamic polarization curves, EIS, hydrogen evolution tests and MTS colorimetric assay using L929 cells on 100 nm thick ALD HfO_2 coated AZ31 samples. This could open the avenue for the use of new coating materials for degradable Mg alloys used as implant material.

2. Materials and methods

2.1. Materials and environment

Commercially available bars of AZ31 Mg alloy were purchased from Dynamic Metals LTD (Leighton Buzzard, UK). More than 500 grains have been considered for the grain analysis by using LAS image software, and a representative image of the microstructure is depicted in Fig. 1. As it can be seen, the material is characterized by a homogeneous α matrix, and the average grain size, obtained by means of linear intercept method, was equal to 13.2 ± 8 μm.

The environment used for the corrosion experiments was simulated body fluid (SBF) prepared according to Ref. [44], while that used for the cytotoxicity experiments was Dulbecco's Modified Eagle Medium (DMEM – Life Technologies Corp, California, USA) supplemented with 10%v/v fetal

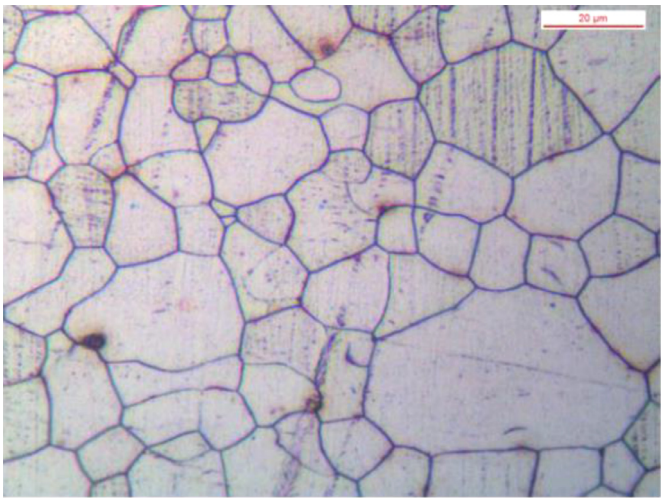

Fig. 1. Micrography of the AZ31 alloy microstructure.

bovine serum (FBS), 100 µg/ml streptomycin and 100 U/ml penicillin.

2.2. Atomic layer deposition

A commercial ALD reactor (Savannah S200, Veeco Instruments Inc., Massachusetts, USA) was used to deposit the ALD coatings. The deposition was carried out through successive cyclic reactions. In particular, 926 successive cyclic reactions between Tetrakis (dimethylamino) zirconium (TDMAZ) and deionized water (H_2O) were used to deposit 100 nm of ZrO_2 (deposition rate of approximately 1.08 Å/cycle), at a temperature of 160 °C. Each cycle was composed of two parts:

(1) 250-ms TDMAZ precursor pulse followed by a 10-s Hi-purity N_2 purge with a flow rate of 20 sccm.
(2) 150-ms H_2O precursor pulse followed by a 15-ms Hi-purity N_2 purge.

The N_2 purge was used to remove residual reactants and by-products from the chamber so as to prevent any additional chemical vapor deposition reactions. During the deposition process, the TDMAZ precursor was heated at 75 °C, while the H_2O precursor and the delivery lines were kept at 25 °C and 160 °C, respectively. Concerning TiO_2, the metal organic precursor used was Tetrakis (dimethylamino) titanium (IV) or TDMA-Ti heated at 75°C. Each cycle was again composed of two parts:

(1) 0.1 s TDMA-Ti precursor pulse followed by a 5 s Hi-purity N_2 purge with a flow rate of 20 sccm.
(2) 0.015 s H_2O precursor pulse followed by a 5 s Hi-purity N_2 purge.

The deposition rate was found to be 0.5 A˚/cycle. Finally, the deposition of HfO_2 was carried out through successive cyclic reactions between Tetrakis (dimethylamino) Hafnium (TDMAH) and deionized water (H_2O) at 160 °C. Again, each cycle was composed of two parts:

(1) 200-ms TDMAZ precursor pulse followed by a 10-s Hi-purity N_2 purge (flow rate of 20 sccm).
(2) 150-ms H_2O precursor pulse followed by a 10 s Hi-purity N_2 purge.

During the deposition process, the TDMAZ precursor was heated at 75 °C, while the H_2O precursor and the delivery lines were kept at 25 °C and 160 °C, respectively. The deposition rate was measured at 1.3 Å/cycle. All the chemical precursors have been supplied by Sigma Aldrich (St. Louis, Missouri, USA).

2.3. Coating characterization

X-ray photoluminescence (XPS) measurements were conducted to assess the chemical composition of the TiO_2, ZrO_2 and HfO_2 ALD coatings. To do so, a Kratos Analytical XPS Microprobe (Kratos Analytical Ltd, Manchester, UK) using Al (Kα) radiation of 1486 eV in a vacuum environment of 5×10^{-9} Torr was used. The XPS data were analyzed using CasaXPS software.

2.4. Corrosion experiments

The corrosion performances of coated and uncoated AZ31 alloy have been characterized by means of potentiodynamic polarization curves, electrochemical impedance spectroscopy and hydrogen evolution tests. The environment used for the corrosion experiments was simulated body fluid (SBF) prepared according to Ref. [44].

2.4.1. Potentiodynamic polarization curves

The commercially available bars were machined into discs with a thickness of 2 mm and a diameter of 29 mm. The discs were then grounded with 2000 grit silicon carbide papers. Afterwards, the samples were cleaned with acetone for five minutes in ultrasonic bath and subsequently with ethanol using the same procedure. A Gamry Reference 600+ potentiostat was used to obtain the potentiodynamic polarization curves of bare and coated samples. A three-electrode setup was used, with the bare or coated samples being the working electrode, the Hg/Hg_2SO_4 electrode being the reference electrode, and the platinum plate electrode being the counter electrode. Static simulated body fluid (SBF) with a pH of 7.4 and at a temperature of 37 °C was used as electrolyte. The surface area of the samples exposed to the SBF was 1 cm^2. Before carrying out the potentiodynamic polarization tests, 30 min were waited to achieve a stable open-circuit potential. The potentiodynamic polarization tests were carried out at a scan rate of 0.5 mV/s, and the tests were repeated three times for each condition.

2.4.2. Electrochemical impedance spectroscopy

Electrochemical impedance spectroscopy was carried out using the same three-electrode configuration and the same

potentiostat as described in the previous Section. Additionally, the electrochemical cell was placed inside a Faraday's cage to avoid noise in the results. To fit the results, the software Gamry Echem Analyst (Gamry Instruments, Warminster, PA, USA) was used. The signal amplitude during EIS was 10 mV relative to the open circuit potential (OCP) at a frequency range of 10^{-2} to 10^{5} Hz, and the samples were kept in SBF for half an hour before measurements to stabilize and measure OCP. The tests were repeated three times for each condition.

2.4.3. Hydrogen evolution tests

Mg, when in contact with an aqueous environment, leads to the evolution of hydrogen gas according to the following equation [2]:

$$Mg + 2H_2O \rightarrow Mg(OH)_2 + H_2 \quad (1)$$

Specifically, the dissolution of one mole of magnesium leads to the release of one mole of hydrogen. It is hence clear that it is possible to measure the corrosion rate of Mg and its alloys by measuring the evolved hydrogen. The use of this method, besides being simple, allows to overcome the limitations of the weight loss method and of the electrochemical techniques [45]. To perform such experiments, the commercially available bars were machined into cubic samples of 5 mm side and they were then prepared as described in Section 2.4. Finally, the samples were immersed in SBF at 37 °C for 7 days and the hydrogen bubbles were collected into a burette according to the procedure reported in Ref. [45]. The tests were repeated three times for each condition.

2.5. Degradation behavior

Micro- and macro-morphological characterizations of bare and coated samples were carried out by means of FEI Quanta 450 Scanning Electron Microscope (Thermo Fisher Scientific Inc., USA) and Canon EOS 4000D (Canon, Tokyo, Japan), respectively. To do so, cylindrical samples were prepared as described in Section 2.4. The samples were characterized before and after corrosion, having been soaked in SBF at 37 °C for one day.

2.6. Cytotoxicity testing

Cytotoxicity was assessed via the MTS cell proliferation assay (Promega) in L929 murine fibroblasts as per manufacturer's recommendations. To compare the cytocompatibility of the different coatings, extracts were prepared by incubating the samples in Dulbecco's Modified Eagle Medium (DMEM – Life Technologies Corp, California, USA), supplemented with 10%v/v fetal bovine serum (FBS), 100 U/ml penicillin and 100 µg/ml streptomycin (complete DMEM) with 1.25 ml/cm^2 extraction ratio for 72 h at 37 °C in a humidified atmosphere with 5% CO_2 [46,47]. The supernatants were collected and centrifuged, and 100% extracts were employed for the cell proliferation assay. Briefly, 3×10^3 cells/well were seeded on 96-well plates and incubated for 24 h to allow attachment. Starting from the following day, 100 µl of the different extracts were added to each well. Complete DMEM was applied as a negative control. The effect of the extracts on cell viability was assessed after 1, 3 and 5 days of treatment. The generation of colored formazan by reduction of the MTS tetrazolium compound was monitored by measuring absorbance at 490 nm on a VICTOR^{TM}X3 plate reader (Perkin Elmer, Massachusetts, USA).

In addition, another set of samples was incubated as just described to assess the pH evolution of the extracts with a pH meter Inolab 730 (WTW, Weilheim, Germany).

3. Results

3.1. Coating characterization

XPS was conducted to determine the chemical composition of the ALD deposited TiO_2, ZrO_2 and HfO_2. In order to have minimum effect of the underlying substrate, the measurements were carried out on thin film deposited on Si wafer. Prior to chemical characterization, the effect of environmental contamination and surface oxidation were removed by etching the surface for three minutes with an energy of 2 KeV. Dealing with titania, high resolution regional scans were carried out for titanium, oxygen and carbon. The negligible amount of carbon detected excluded the presence of any process contamination, thus indicating an ideal deposition. Regional scans of titanium and oxygen are reported in Fig. 2(a) and (b), respectively. Particularly, from the regional scan of titanium, peaks corresponding to the core level binding energies of Ti $2p_{3/2}$ and Ti $2p_{1/2}$ (i.e., 459 eV and 464 eV, respectively) can be observed, indicating the presence of Ti^{4+} oxidation state in TiO_2 [48]. Moreover, the presence of Ti^{3+} due to the argon etching step caused the shoulder at lower energy around 456 eV is due to [49]. Dealing with oxygen, oxygen atoms in TiO_2 phase lead to the peak at 531 eV [50], while the oxygen in hydroxyl groups present in the form of impurities induces the small shoulder at higher energy. From a composition perspective, we found an oxygen deficient deposition since we found 60% of oxygen and 40% of titanium, while the stochiometric composition should be 66.7% oxygen and 33.3% titanium (Ti and oxygen in 1:2 ratio).

With respect to zirconia, regional scans of zirconium, oxygen and carbon were also carried out at high resolution. No peak was observed in the high resolution scan for the element carbon, thus showing a nearly carbon-free ALD deposition. The high resolution spectra (Fig. 3a) of Zr 3d showed two peaks at binding energy 182 eV and 184 eV, which correspond to Zr $3d_{5/2}$ and Zr $3d_{3/2}$, respectively. The scan conducted for O 1 s (Fig. 3b) showed a peak at 530 eV which belongs to ZrO_2 and the shoulder on the higher energy side is due to the oxidation of metal in air forming ZrO. The quantification calculation using CASAXPS software showed a composition as 40% Zr and 60% O, indicating an oxygen deficient zirconia thin film.

Finally, dealing with hafnia, high resolution regional scans for hafnium, oxygen and carbon were carried out. Again, an

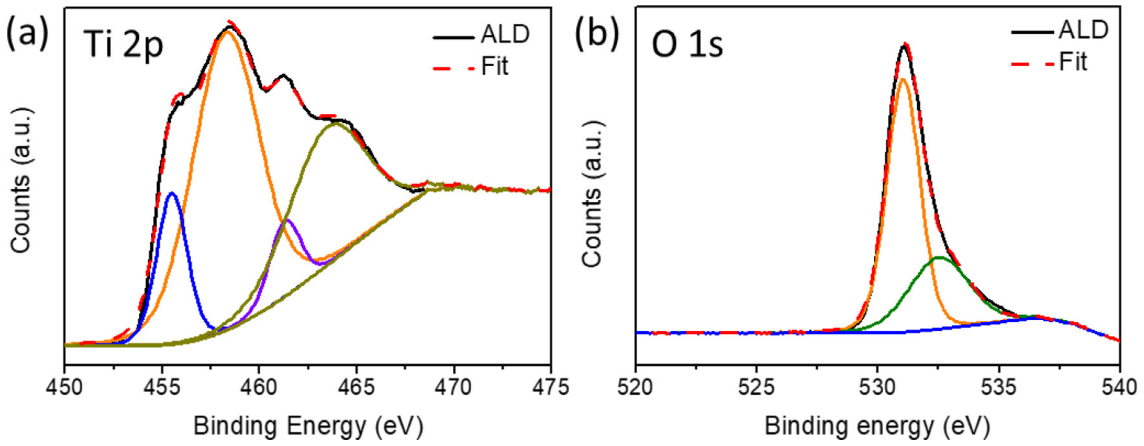

Fig. 2. XPS spectra for ALD deposited TiO_2 (a) Ti 2p (b) O 1 s.

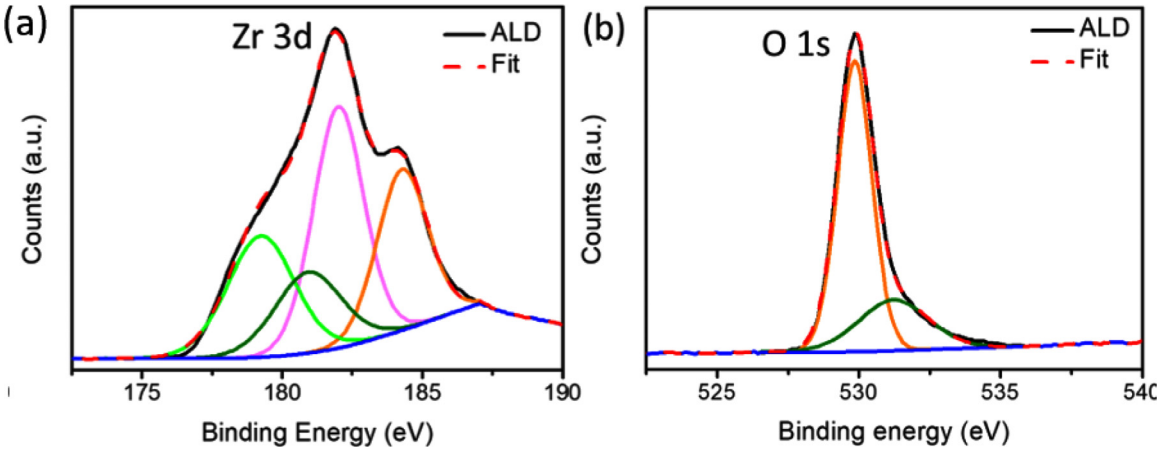

Fig. 3. XPS spectra for ALD deposited ZrO_2 (a) Zr 3d (b) O 1 s.

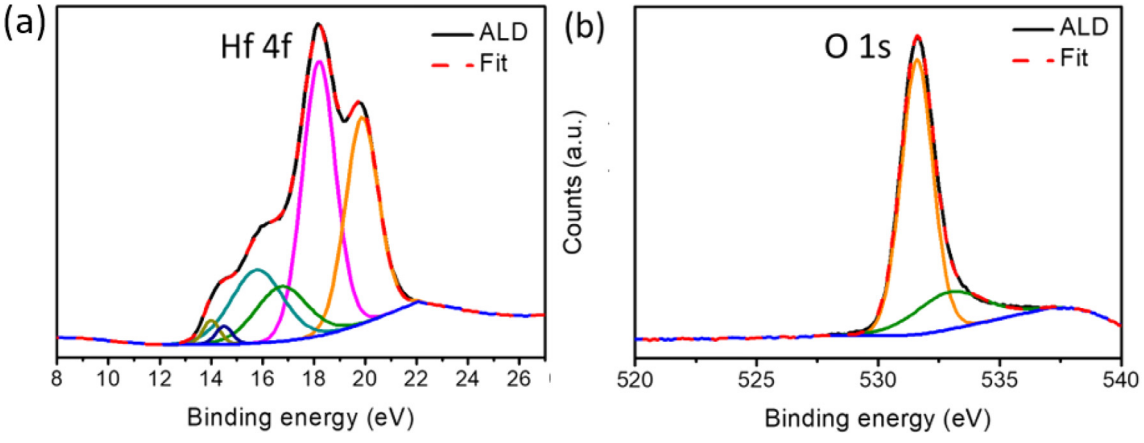

Fig. 4. XPS depth profile spectra of ALD deposited HfO_2 (a) Hf 4f and (b) O 1 s.

ideal deposition without any contaminants was highlighted by the negligible amount of carbon detected. Fig. 4b shows the core level spectra of O 1 s associated with HfO_2 [51]. The region at higher energy above the peak at 531 eV shows a shoulder due to presence of a small amount of contamination, likely carbon or moisture. In the regional scan of element Hf 4f, peak positions at 18.5 eV and 20.7 eV correspond to Hf $4f_{7/2}$ and Hf $4f_{5/2}$ in HfO_2 [52]. The shoulders at lower energies below 18.5 eV are due to Hf interstitials and oxygen vacancies [53]. Again, we observed an oxygen deficient deposition. In fact, we observed a composition of 63% oxygen and 37% hafnium, while the stoichiometric composition of HfO_2 should have Hf and O in 1:2 ratio i.e. 66.7% oxygen and 33.3% hafnium.

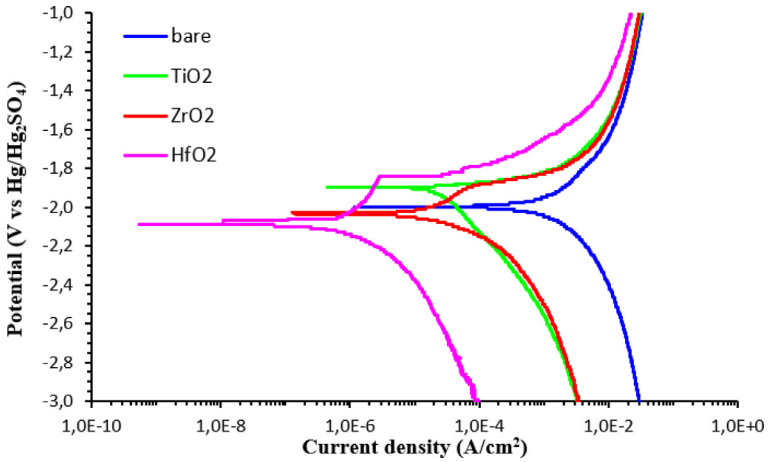

Fig. 5. Potentiodynamic polarization curves of bare (blue), TiO_2 (green), ZrO_2 (red) and HfO_2 (fuchsia) AZ31 alloy in SBF. (For interpretation of the references to colour in this figure legend, the reader is referred to the web version of this article.)

Table 1
Corrosion potentials (E_{corr}) and corrosion current densities (i_{corr}) values for bare and coated AZ31 samples in SBF.

	Bare	TiO_2 coating	ZrO_2 coating	HfO_2 coating
E_{corr} (V)	-2.0 ± 0.02	-1.90 ± 0.01	-2.02 ± 0.01	-2.09 ± 0.02
i_{corr} (A/cm^2)	$3.0\ 10^{-3} \pm 0.4$	$24.9\ 10^{-6} \pm 0.6$	$1.2\ 10^{-6} \pm 0.3$	$0.6\ 10^{-6} \pm 0.4$

3.2. Corrosion experiments

3.2.1. Potentiodynamic polarization curves

Fig. 5 reports the potentiodynamic polarization curves of bare and coated samples. Moreover, the average values of the corrosion potentials (E_{corr}) and of the corrosion current densities (i_{corr}) are reported in Table 1. In the light of the well-known relation between the corrosion resistance of a sample and the observed values of the corrosion current density and of the corrosion potential (i.e., the lower the corrosion current density, the lower the corrosion rate, and the higher the corrosion potential, the lower the tendency to corrode), it can be observed that the presence of the coatings increases the corrosion resistance of the material. In particular, the HfO_2 coating is reported to provide the lowest corrosion current density, that is half of that provided by ZrO_2 and 40 times lower than that of TiO_2.

3.2.2. Electrochemical impedance spectroscopy

The Nyquist-plots of bare and TiO_2, ZrO_2, and HfO_2 coated samples are shown in Fig. 6a, b, c and d, respectively. It is worth mentioning that, for sake of clarity, the Figures are characterized by different axis scales. In the Nyquist plots, the bare and the coated samples are characterized by three time constants being the capacitive loop in the high and medium frequency range (related to the charge transfer process between the base and the coatings) and the inductive loop in the low-frequency range (related to the superficial corrosion state of AZ31 alloy in the solution) [54,55]. Being the capacity loop connected to the transfer process between the coating and the substrate, a larger capacitive loop means better corrosion resistance [56]. Due to the larger diameter of the capacitive loops of the coated samples compared to the bare sample, the treated samples show much better performance in corrosion resistance. The capacitive loops and hence the corrosion performance are ranked $HfO_2 > ZrO_2 > TiO_2 >$ bare, confirming the results of the potentiodynamic polarization curves. There is a large difference in impedance among the different samples, as can be seen by inspecting the order of magnitudes on the axes.

The Bode plots of bare and TiO_2, ZrO_2, and HfO_2 are shown in Fig. 7a, b, c and d, respectively. The Bode plots also help to investigate the corrosion resistance, as a higher value of $|Z|_{f\to 0}$ means greater corrosion resistance [57,58]. The $|Z|_{f\to 0}$ value for the bare, TiO_2, ZrO_2 and HfO_2 coated samples is $1.4 \cdot 10^2\ \Omega \cdot cm^2$, $4.5 \cdot 10^3\ \Omega \cdot cm^2$, $2.1 \cdot 10^6\ \Omega \cdot cm^2$ and $4 \cdot 10^7\ \Omega \cdot cm^2$, respectively, confirming the results found in the Nyquist plots.

3.2.3. Hydrogen evolution tests

Fig. 8 reports the results of the hydrogen evolution tests from bare and coated samples. In agreement with the results of the potentiodynamic polarization tests and of the electrochemical impedance spectroscopy, the hydrogen evolution experiments further suggest that the application of the coatings can prevent the degradation of AZ31 alloy. In particular, after 7 days, the hydrogen evolved from the bare samples is reduced by 52% if 100 nm of ALD TiO_2 is considered. Higher improvements are obtained if ZrO_2 and, above all, HfO_2 are employed: the former leads to a reduction in the hydrogen evolved by 92.5%, while the latter to a reduction by 95%.

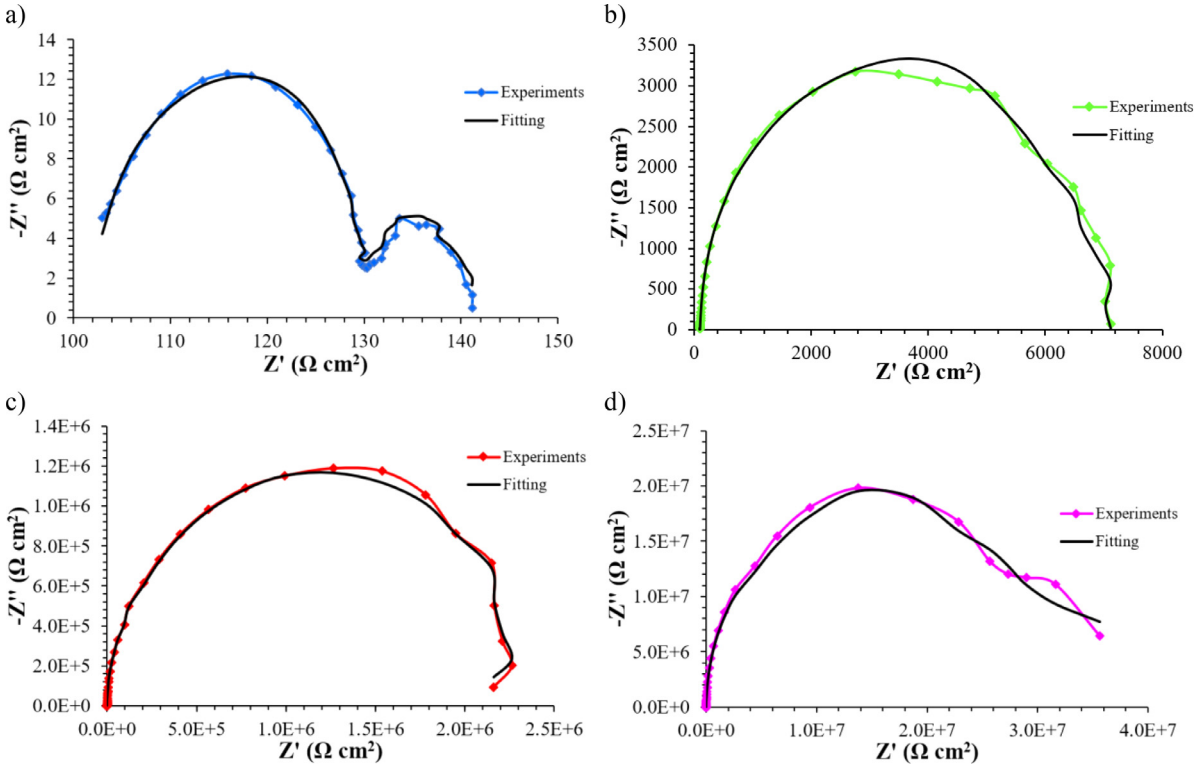

Fig. 6. Nyquist plots of bare (a), TiO_2 (b), ZrO_2 (c) and HfO_2 (d) coated AZ31 alloy in SBF.

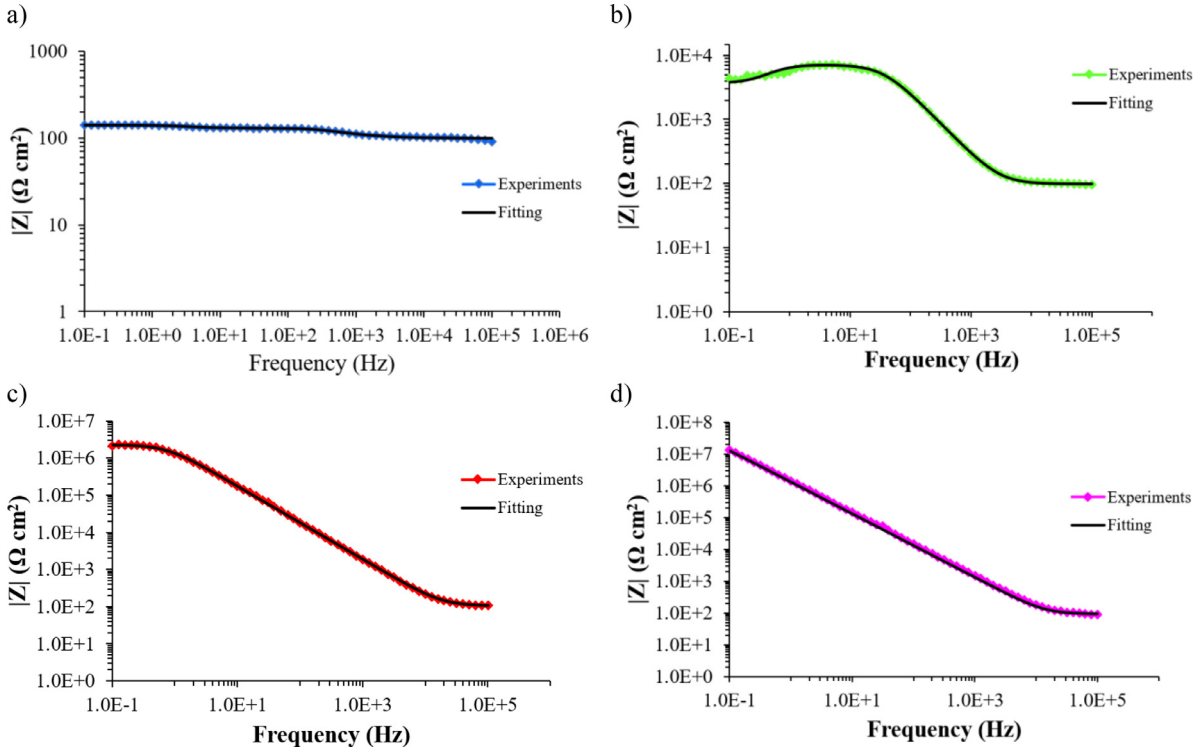

Fig. 7. Bode plots of bare (a), TiO_2 (b), ZrO_2 (c) and HfO_2 (d) coated AZ31 alloy in SBF.

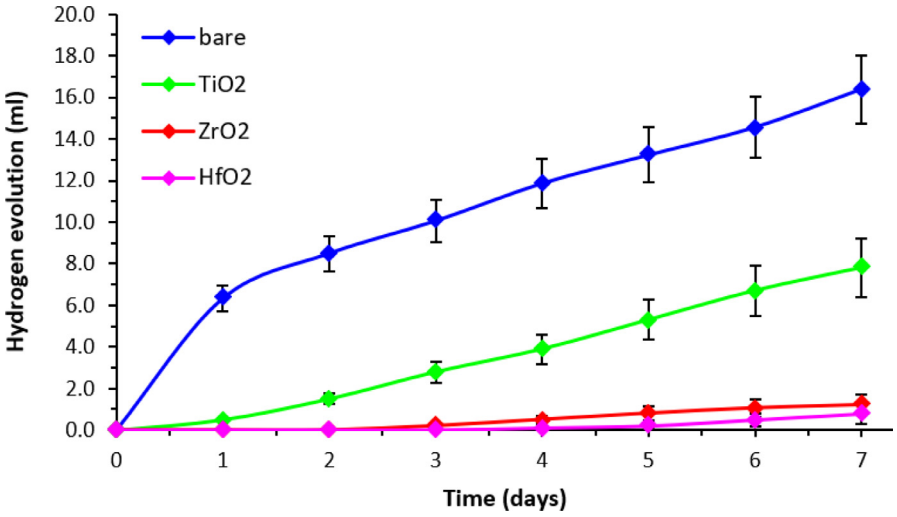

Fig. 8. Hydrogen evolved from the immersion of bare and coated AZ31 alloy in SBF.

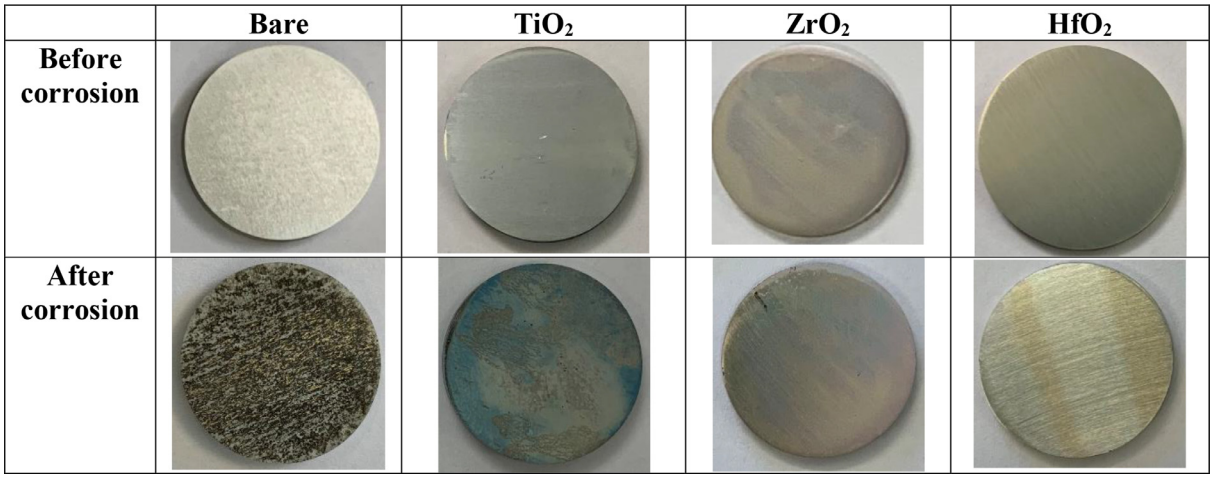

Fig. 9. Macro-morphologies of bare, TiO_2, ZrO_2 and HfO_2 coated samples before and after corrosion.

It is interesting to note the behavior of the bare samples. After a first phase where the hydrogen evolution rate is high, the slope of the curve highly reduces. This is linked to the presence of corrosion products. At first, in fact, the bare alloy is covered by a surface layer of MgO and/or $Mg(OH)_2$ that spontaneously form. This surface layer is however very soluble in water environment, hence the corrosion rate is high. With the continuation of the surface process, the pH increase leads to the precipitation of Ca-phosphate on the surface, which is protective, and determines a reduction of the corrosion rate [59].

3.3. Degradation behavior

Fig. 9 displays the macro-morphologies of coated samples before and after being soaked for one day in SBF. The bare AZ31 sample was employed as control.

It is clearly observable from the figure that the application of coatings reduced the corrosion damage. Particularly, in the case of HfO_2 coated samples, the corrosion damage became negligible. The extensively corroded surface of bare samples, characterized by pits, was reduced by applying a TiO_2 layer, where un-corroded areas were accompanied by corroded areas characterized by a filiform corrosion. Barely any corrosion apart from the small area at the edge of the sample was observable from the macro-morphologies of ZrO_2 coated samples. However, the micro-morphologies revealed some small corroded area in the center of the ZrO_2 coated samples (Figs. 10h and i). In addition, although the macro-morphologies of HfO_2 coated samples did not reveal any corrosion, the micro-morphologies showed the presence of some small areas where the early stage of the corrosion products formation can be seen, together with the onset of filiform corrosion (Figs. 10k and l). TiO_2 coated samples and bare samples are characterized by a large number of cracks dividing the surface into network structure (Figs. 10b and c and Figs. 10e and f for bare and TiO_2 coated samples, respectively). In addition, in the bare samples, the surface film layer began to delaminate and flake off (Figs. 10b and c).

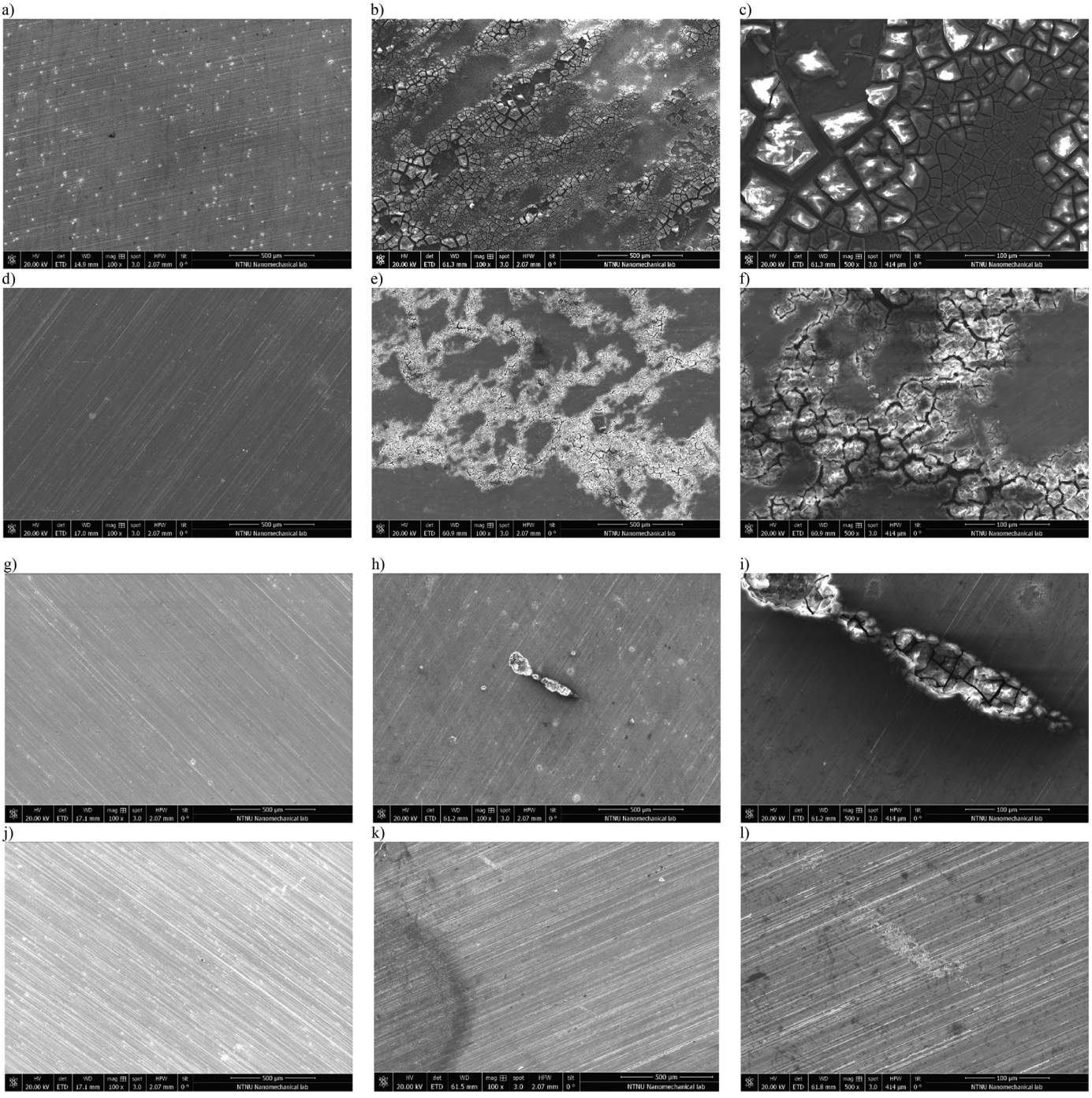

Fig. 10. Micro-morphologies of bare (b and c), TiO_2 (e and f), ZrO_2 (h and i) and HfO_2 (k and l) coated samples after corrosion. Micro-morphologies of samples before corrosion are also reported (a, d, g and j for bare, TiO_2, ZrO_2 and HfO_2 coated samples, respectively).

3.4. Cytotoxicity testing

The MTS assay was performed on L929 murine cell line to determine the cytotoxicity of the different ALD coatings. Fig. 11 shows the viability of L929 cells after exposure to extracts of the AZ31 alloy and coated samples after 1, 3 and 5 days in culture (Fig. 11).

Finally, Fig. 12 reports the pH evolution during the preparation of the extracts.

As it can be observed, the application of the coatings can lower the increase in pH produced by the bare alloy. In particular, the pH is reduced by 15.5% if 100 nm of ALD TiO_2 is considered. Higher improvements are obtained if ZrO_2 and, above all, HfO_2 are employed: the former leads to a reduc-

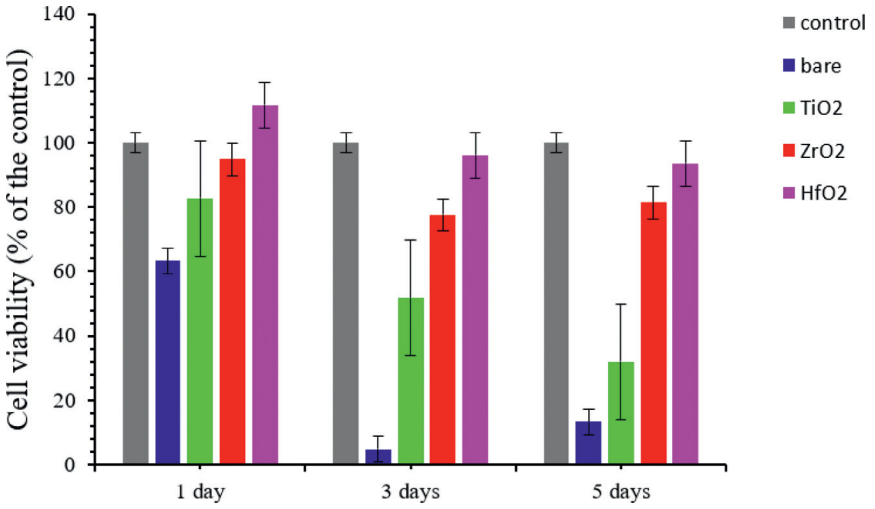

Fig. 11. Cell viability of L-929 cultured in extracts from bare and coated AZ31 substrates after culture for 1, 3 and 5 days. Error bars represent means ± SEM for $n=3$. (For interpretation of the references to colour in this figure legend, the reader is referred to the web version of this article.)

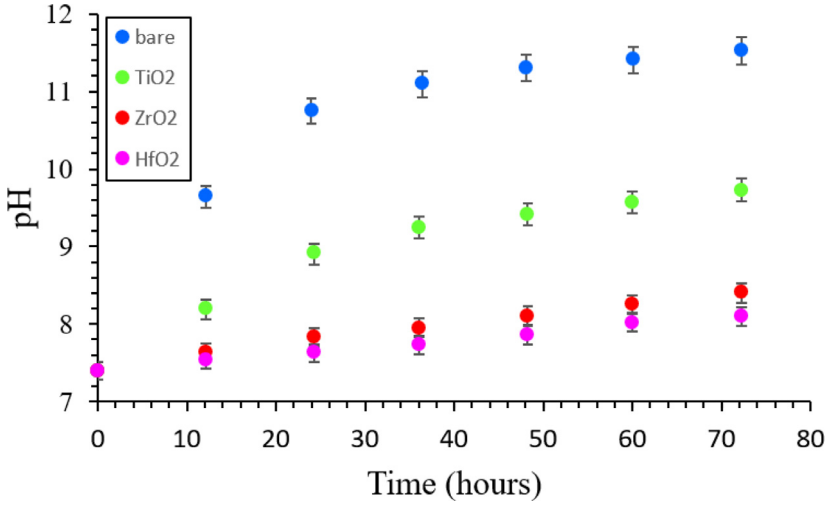

Fig. 12. pH evolution of bare and coated samples in DMEM supplemented with 10% FBS and penicillin/streptomycin.

tion in the hydrogen evolved by 27.1%, while the latter to a reduction by 29.7%.

4. Discussion

In this work, we aimed to evaluate the effects of three biocompatible ALD coatings (TiO_2, ZrO_2 and HfO_2) on the corrosion resistance and cytotoxicity of AZ31 alloy. Particularly, being Mg and its alloys optimal materials for temporary implants, the impact of the corrosion products on cell viability in the immediate surrounding of the implant represents one of the most important aspects to take into consideration. In the light of this, MTS colorimetric assays with L929 cells were used to evaluate the effect of sample extracts on cell viability. As shown in Fig. 11, the application of coatings increases the cell viability of the bare AZ31 alloy. Specifically, HfO_2 coating is found to lead to the highest improvements, while TiO_2 to the lowest. However, according to the evaluation of cytotoxicity listed in Table 2, not all the coatings lead to Grade 1 cytotoxicity, that represents the threshold above which a material is considered to meet the demands for cellular applications [60].

Table 2
The standard evaluation of cytotoxicity (%).

Cell viability	≥100	75–99	50–74	25–49	1–24	<1
Grade	0	1	2	3	4	5

In fact, Grade 1 cytotoxicity was constantly found only for ZrO_2 and HfO_2, with the latter to be the only one showing Grade 0 cytotoxicity at day 1. TiO_2 coatings are instead characterized by Grade 1 cytotoxicity only at 1 day of culture, after that the viability decreases to Grade 2. Considering bare samples, they are always characterized by a too low viability to meet the demands for cellular applications. Detailed results are reported in Table 3.

The different cell viability degrees shown by the coated and uncoated samples can be related to the different pH of

Table 3
Classification of the observed cytotoxicity of uncoated and coated AZ31 alloys. The cell viability corresponding to the coating type is reported in brackets.

Cytotoxicity Grade	0	1	2	3	4	5
Viability at 1 day of culture	HfO_2 (111.6%)	ZrO_2 (94.8%) TiO_2 (82.8%)	Bare (63.4%)			
Viability at 3 day of culture		HfO_2 (96.1%) ZrO_2 (77.6%)	TiO_2 (51.7%)		Bare (4.7%)	
Viability at 5 day of culture		HfO_2 (93.5%) ZrO_2 (81.5%)		TiO_2 (31.9%)	Bare (13.4%)	

the extracts. A pH higher than 9 has in fact been reported to inhibit the proliferation of L929 cells [61]. In the light of this, the pH of the extracts reported in Fig. 12 can, at least partially, explain the different Cytotoxicity Grades. Specifically, ZrO_2 and HfO_2 coatings are the only ones characterized by Grade 1 cytotoxicity, and they indeed always show a pH lower than 9. In particular, HfO_2 coating is the only one showing Grade 0 cytotoxicity as a consequence of the lowest increase in pH. The correlation of the Cytotoxicity Grades with the pH is even more evident in the case of TiO_2 coatings: when the pH of the extracts is lower than 9 (after 1 day of culture), the TiO_2 coatings can meet the demands for cellular applications, whereas, when the pH of the extracts is higher, the proliferation of the L929 cells is inhibited, thus resulting in Grade 2 and 3. Finally, bare samples are characterized by a pH higher than 9 also after 1 day of culture, thus explaining the reported high Cytotoxicity Grades.

To pH behavior can then be linked to the corrosion behavior: the increase in the pH is in fact due to the evolution of OH^- ions from the corrosion process of Mg and its alloys, and the lower the corrosion resistance, the higher the increase of the pH. The corrosion resistance has herein been evaluated in three different ways, i.e. through potentiodynamic polarization curves, EIS spectra and hydrogen evolution experiments. Starting from the potentiodynamic polarization curves, the most important parameter to be considered is the corrosion current density. Specifically, the corrosion current density is directly related to the corrosion rate (i.e., the lower the corrosion current density, the lower the corrosion rate). From Fig. 5 and Table 1, it can be seen that the corrosion current density of the bare sample is decreased by three orders of magnitude. In particular, the HfO_2 coating is reported to provide the lowest corrosion current density, with the corrosion resistance following the trend $HfO_2 > ZrO_2 > TiO_2 >$ bare. More in detail, the corrosion current density of HfO_2 is half of that provided by ZrO_2 and 40 times lower than that of TiO_2. A similar trend can be found considering the hydrogen evolution test and the EIS spectra. Dealing with the former, Fig. 8 shows that HfO_2 coating reduces the hydrogen evolved from the bare sample by 95%. A similar, but lower, reduction (92.5%) is achieved when considering ZrO_2 coating, while a much lower reduction (52%) is provided by TiO_2 coating. Dealing with the EIS spectra (Fig. 6), then, the diameters of the capacitive loops of the Nyquist-plots confirm the corrosion trend again: the higher the diameter of the capacitive loops (and equivalently the value of $|Z|_{f\to 0}$), in fact, the higher the corrosion resistance. Moreover, the EIS spectra

Table 4
Fitting results for EIS Spectra.

	Bare	TiO_2	ZrO_2	HfO_2
R_s (Ω cm^2)	100.16	98.42	106.40	95.0
R_1 (Ω cm^2)	9.34	2.63×10^3	1.64×10^{11}	3.30×10^7
C_1 (Ω^{-1} cm^{-2} s^{-n})	5.71×10^{-3}	1.29×10^{-4}	1.05×10^{-5}	1.29×10^{-7}
Q_1 (Ω^{-1} cm^{-2} s^{-n})	7.07×10^{-5}	7.24×10^{-7}	9.71×10^{-8}	1.30×10^{-6}
n	0.748	0.938	0.984	1
R_2 (Ω cm^2)	3.79×10^1	6.88×10^3	2.25×10^6	3.80×10^7
R_L (Ω cm^2)	1.78×10^2	1.05×10^3	3.21×10^{-1}	1.71×10^6
L (H cm^2)	1.84×10^{-1}	2.35×10^{-3}	2.42×10^7	1.25×10^7

are particularly interesting to better understand the corrosion process. The EIS spectra of each material indicate, in fact, its specific electronic transportation process. This can be simulated by an equivalent circuit (EC). In this work the EC used is that suggested in previous works on ALD [25,62] and it is reported in Fig. 13.

R_s, R_1 and R_2 represent the electrical impedance of the electrolyte, the surface modification layer (MgO in the case of bare samples), and the charge transfer resistance respectively. C_1 represents the capacitance of either the coatings or the surface corrosion products of the bare AZ31. R_L and L represent the resistance and inductance of the species absorbed into the coating, respectively [63]. Q_1 acts as a constant phase element (CPE) of the electric double layer on the electrode surface [56]. Yang et al. reported that high values for R_1 and R_2 and low values for Q_1 and C_1 are characteristics of a better corrosion resistance [62], and, from the fitting results (Table 4), it can be seen that all the coated samples exhibit higher corrosion resistance than the bare samples (due to higher values for R_1 and R_2 and lower values for Q_1 and C_1).

Moreover, they also stated that R_1 and R_2 are directly related to the integrity of the coating. Therefore, to understand the different corrosion performances, the coating integrities need to be considered together with their electrochemical properties. Dealing with the former, the presence of defects such as cracks and pores are known to affect the corrosion behavior inducing filiform corrosion (Fig. 10) and to reduce the protectiveness of the coating allowing a path for the fluid to enter the material [64]. Cracks are known to form as a consequence of the induced residual stresses on the coating due to the different thermal expansion coefficient of the coating and of the substrate [65,66]. Mg, in fact, is reported to have a coefficient of thermal expansion of $27{\cdot}10^{-6}\ °C^{-1}$ [67], while TiO_2, ZrO_2 and HfO_2 of $7{\cdot}10^{-6}\ °C^{-1}$, $11{\cdot}10^{-6}\ °C^{-1}$ and

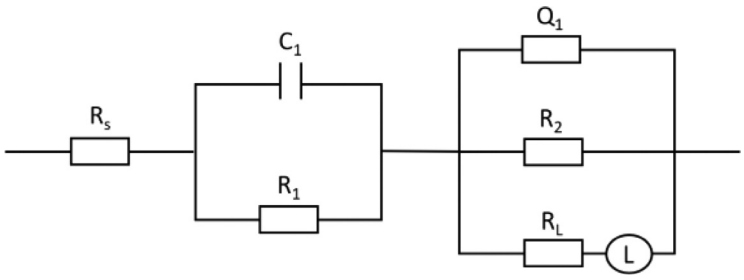

Fig. 13. Equivalent Circuit for EIS spectra.

Table 5
Polarization resistance of bare and coated samples.

	Bare	TiO_2	ZrO_2	HfO_2
Polarization Resistance (Ω cm^2)	42.9	7.0 10^3	2.3 10^6	3.8 10^8

$10{\cdot}10^{-6}\ {}^{\circ}C^{-1}$, respectively [68–70]. The mismatch between the substrate and the coating is lower with ZrO_2 and higher with TiO_2. This would suggest ZrO_2 coating to provide the highest corrosion resistance among the considered materials. However, the results herein reported showed that the highest improvements in terms of corrosion resistance were provided by the HfO_2 coatings. This can be linked to the lower porosity of the HfO_2 compared to ZrO_2 and, even more, to TiO_2. Elsener et al. [71] proposed an electrochemical method to estimate the porosity of thin films based on the following Equation:

$$Porosity = \left(\frac{R_{p,s}}{R_p}\right) \cdot 10^{-\frac{\Delta E_{corr}}{b_a}} \quad (2)$$

Where $R_{p,s}$ and R_p are the polarization resistances of the bare and coated material in Ωcm^2, respectively, ΔE_{corr} is the change of the corrosion potential caused by the presence of the coating layer in mV and b_a is the anodic Tafel slope of the bare substrate in mV/decade. The polarization resistances, corresponding to the diameter of the capacitive loop in the Nyquist plots, are reported in Table 5, the ΔE_{corr} can be measured from the results of the potentiodynamic polarization curves reported in Table 1, and the anodic Tafel slope of the bare substrate was measured equal to 442 mV/decade from the potentiodynamic polarization curves. The corresponding porosity was found to be 0.36%, 0.0016% and 0,00,007% for TiO_2, ZrO_2 and HfO_2, respectively.

Another reason for the better corrosion resistance of HfO_2 is the difference in cohesive energies [72]. In fact, the higher the cohesive energy, the more electrochemically stable is the material and thus, the lower its corrosion. The cohesive energy of HfO_2 is the highest among the three materials herein studied, while TiO_2 is the lowest [73]; the cohesive energy of ZrO_2 is instead slightly lower than that of HfO_2 and this could explain the different corrosion behavior observed. Finally, the lower wettability of HfO_2 compared to ZrO_2 and TiO_2 further explains the herein reported corrosion behavior [74–76] and hence the cell viability results.

It is worth mentioning that, with respect to the biocompatibility of TiO_2, the results herein reported differ from what is known from the literature. In fact, TiO_2 is widely known as one of the most biocompatible materials since it induces fast deposition of apatite from SBF in vitro and stimulates the adhesion and proliferation of cells [77,78]. However, although the biocompatibility of TiO_2 remains undisputed when the cells are in direct contact, biocompatibility issues may arise when TiO_2 is used as coating material for Mg and its alloys, and it is not effective in reducing the corrosion rate of the magnesium substrate leading to an environment that reveals to be toxic for the cells due to the increase in the pH and to the high concentration of Mg^{2+} ions.

Therefore, in the choice of a coating material for degradable Mg alloys used as implant material, it is important to consider its cohesive energy, wettability, porosity and thermal expansion coefficient to provide an effective reduction of the corrosion rate of the Mg substrate that otherwise would affect the biocompatibility of the coating itself, creating a lethal environment for cells and tissues.

5. Conclusions

In this study, the effects of a 100 nm thick TiO_2, ZrO_2 and HfO_2 ALD coating on the corrosion behavior and on the cytotoxicity of the AZ31 Mg alloy were assessed. To this regard, potentiodynamic polarization curves, EIS and hydrogen evolution experiments have been carried out to assess the former, while MTS proliferation assay using L929 cells to assess the latter. Whereas the presence of TiO2 coatings is reported to improve the corrosion performances with respect to the bare AZ31 alloys, ZrO_2 and, above all, HfO_2 ALD coatings provide a significantly higher corrosion resistance. This can be explained considering their lower wettability, their higher electrochemical stability and their higher surface integrity (i.e., less cracks and pores). This improved corrosion resistance has positive effects on the cytotoxicity of AZ31 alloy. Indeed, the reduced corrosion provided by the coatings leads to a lower increase in the pH and in the concentration of Mg^{2+} ions, inducing the cytotoxicity Grade to move from Grade 4 for bare AZ31 alloy to Grade 2 for TiO_2 coating and to Grade 1 for ZrO_2 and HfO_2 coatings. In particular, HfO_2 coating was also found to report a Grade 0 cytotoxicity considering the extracts assessed at 1 day of culture. As a grade 1 toxicity is the minimum requirement

for FDA approval, the choice of the appropriate coating has to include a cytotoxicity benchmark of its corrosion products and cannot be linked to the assessment of cell attachment to the biomaterial surface only.

Declaration of Competing Interest

None.

References

[1] M.P. Ginebra, T. Traykova, J.A. Planell, J. Control. Release. 113 (2006) 102–110, doi:10.1016/j.jconrel.2006.04.007.

[2] M. Peron, J. Torgersen, F. Berto, Metals (Basel) 7 (2017) 252, doi:10.3390/met7070252.

[3] N. Li, Y. Zheng, J. Mater. Sci. Technol. 29 (2013) 489–502, doi:10.1016/J.JMST.2013.02.005.

[4] R.K. Singh Raman, S. Jafari, S.E. Harandi, Eng. Fract. Mech. 137 (2015) 97–108, doi:10.1016/j.engfracmech.2014.08.009.

[5] M.P. Staiger, A.M. Pietak, J. Huadmai, G. Dias, Biomaterials 27 (2006) 1728–1734, doi:10.1016/j.biomaterials.2005.10.003.

[6] A.C. Hänzi, A.S. Sologubenko, P.J. Uggowitzer, Int. J. Mater. Res. 100 (2009) 1127–1136, doi:10.3139/146.110157.

[7] Y. Sasaki, G.A. Sathi, O. Yamamoto, Mater. Sci. Eng. C. 77 (2017) 52–57, doi:10.1016/j.msec.2017.03.236.

[8] M. Peron, F. Berto, J. Torgersen, Magnesium and Its Alloys As Implant Materials: Corrosion, Mechanical and Biological Performances, CRC Press LLC, 2020.

[9] F. Witte, V. Kaese, H. Haferkamp, E. Switzer, A. Meyer-Lindenberg, C.J. Wirth, H. Windhagen, Biomaterials 26 (2005) 3557–3563, doi:10.1016/j.biomaterials.2004.09.049.

[10] B. Zberg, P.J. Uggowitzer, J.F. Löffler, Nat. Mater. 8 (2009) 887–891, doi:10.1038/nmat2542.

[11] M. Bobby Kannan, W. Dietzel, C. Blawert, A. Atrens, P. Lyon, Mater. Sci. Eng. A. 480 (2008) 529–539, doi:10.1016/J.MSEA.2007.07.070.

[12] L. Choudhary, R.K. Singh Raman, J. Hofstetter, P.J. Uggowitzer, Mater. Sci. Eng. C. 42 (2014) 629–636, doi:10.1016/J.MSEC.2014.06.018.

[13] M. Peron, P.C. Skaret, A. Fabrizi, A. Varone, R. Montanari, H.J. Roven, P. Ferro, F. Berto, J. Torgersen, J. Mech. Behav. Biomed. Mater. (2020) 103724, doi:10.1016/j.jmbbm.2020.103724.

[14] M. Peron, R. Bertolini, A. Ghiotti, J. Torgersen, S. Bruschi, F. Berto, J. Mech. Behav. Biomed. Mater. 101 (2020) 103429, doi:10.1016/J.JMBBM.2019.103429.

[15] K.T. Rim, K.H. Koo, J.S. Park, Saf. Health Work. 4 (2013) 12–26, doi:10.5491/SHAW.2013.4.1.12.

[16] R. Smeets, B. Stadlinger, F. Schwarz, B. Beck-Broichsitter, O. Jung, C. Precht, F. Kloss, A. Gröbe, M. Heiland, T. Ebker, T. Ebker, Biomed Res. Int. 2016 (2016) 1–16, doi:10.1155/2016/6285620.

[17] T. Albrektsson, A. Wennerberg, Int. J. Prosthodont. 17 (2017) 536–543 n.d. http://www.ncbi.nlm.nih.gov/pubmed/15543910 . (accessed October 30.

[18] R. Bertolini, S. Bruschi, A. Ghiotti, L. Pezzato, M. Dabalà, Procedia CIRP 65 (2017) 7–12, doi:10.1016/J.PROCIR.2017.03.168.

[19] T.S.N. Sankara Narayanan, I.-.S. Park, M.H. Lee, Volume 2, Modification and coating techniques (2020) n.d.

[20] T. Lei, in: Surf. Modif. Magnes. Its Alloy. Biomed. Appl., Elsevier Inc., 2015, pp. 135–150, doi:10.1016/B978-1-78242-078-1.00006-2.

[21] T.F. da Conceição, N. Scharnagl, in: Surf. Modif. Magnes. Its Alloy. Biomed. Appl., Elsevier Inc., 2015, pp. 3–21, doi:10.1016/B978-1-78242-078-1.00001-3.

[22] Q. Li, in: Prev. Magnes. Alloy. A Vol. Woodhead Publ. Ser. Met. Surf. Eng., Elsevier Ltd, 2013, pp. 469–485, doi:10.1533/9780857098962.3.469.

[23] M. Peron, A. Bin Afif, A. Dadlani, F. Berto, J. Torgersen, Surf. Coatings Technol. (2020) 125922, doi:10.1016/j.surfcoat.2020.125922.

[24] I.S. Abela, in: Surf. Modif. Magnes. Its Alloy. Biomed. Appl., Elsevier Inc., 2015, pp. 81–100, doi:10.1016/B978-1-78242-078-1.00004-9.

[25] X. Liu, Q. Yang, Z. Li, W. Yuan, Y. Zheng, Z. Cui, X. Yang, K.W.K. Yeung, S. Wu, Appl. Surf. Sci. 434 (2018) 1101–1111, doi:10.1016/J.APSUSC.2017.11.032.

[26] E. Marin, A. Lanzutti, L. Guzman, L. Fedrizzi, J. Coatings Technol. Res. 9 (2012) 347–355, doi:10.1007/s11998-011-9372-8.

[27] E. Marin, A. Lanzutti, L. Paussa, L. Guzman, L. Fedrizzi, Mater. Corros. 66 (2015) 907–914, doi:10.1002/maco.201408012.

[28] C.X. Shan, X. Hou, K.L. Choy, Surf. Coatings Technol. 202 (2008) 2399–2402, doi:10.1016/j.surfcoat.2007.08.066.

[29] T. Kasuga, H. Kondo, M. Nogami, J. Cryst. Growth. 235 (2002) 235–240, doi:10.1016/S0022-0248(01)01782-1.

[30] X.X. Wang, S. Hayakawa, K. Tsuru, A. Osaka, Biomaterials 23 (2002) 1353–1357, doi:10.1016/S0142-9612(01)00254-X.

[31] M. Uchida, H.-.M. Kim, T. Kokubo, T. Nakamura, APATITE-FORMING ABILITY OF TITANIA GELS WITH DIFFERENT STRUCTURES, Bioceramics, WORLD SCIENTIFIC (1999) 149–152, doi:10.1142/9789814291064_0036.

[32] J.-.M. Wu, S. Hayakawa, K. Tsuru, A. Osaka, J. Am. Ceram. Soc. 87 (2004) 1635–1642, doi:10.1111/j.1551-2916.2004.01635.x.

[33] R. Osman, M. Swain, Materials (Basel) 8 (2015) 932–958, doi:10.3390/ma8030932.

[34] H. Harianawala, M. Kheur, S. Kheur, T. Sethi, A. Bal, M. Burhanpurwala, F. Sayed, Biocompatibility of Zirconia, n.d.

[35] L. Rimondini, L. Cerroni, A. Carrassi, P. Torricelli, Bacterial colonization of zirconia ceramic surfaces: an in vitro and in vivo study., Int. J. Oral Maxillofac. Implants. 17 (n.d.) 793–8. http://www.ncbi.nlm.nih.gov/pubmed/12507238 (accessed January 23, 2020).

[36] M. Peron, A. Bin Afif, A.L. Dadlani, F. Berto, J. Torgersen, J. Mech. Behav. Biomed. Mater. 111 (2020) 104005, doi:10.1016/j.jmbbm.2020.104005.

[37] M. Peron, F. Berto, J. Torgersen, Mater. Des. Process. Commun. 126 (2019) mdp2, doi:10.1002/mdp2.126.

[38] M. Peron, J. Torgersen, F. Berto, in: Procedia Struct. Integr, Elsevier B.V., 2019, pp. 538–548, doi:10.1016/j.prostr.2019.08.198.

[39] C.R. Kruse, M. Singh, S. Targosinski, I. Sinha, J.A. Sørensen, E. Eriksson, K. Nuutila, Wound Repair Regen 25 (2017) 260–269, doi:10.1111/wrr.12526.

[40] L.-.E. Monfoulet, P. Becquart, D. Marchat, K. Vandamme, M. Bourguignon, E. Pacard, V. Viateau, H. Petite, D. Logeart-Avramoglou, Tissue Eng. Part A. 20 (2014) 1827–1840, doi:10.1089/ten.tea.2013.0500.

[41] M. Li, Z.-.X. Jin, W. Zhang, Y.-.H. Bai, Y.-.Q. Cao, W.-.M. Li, D. Wu, A.-.D. Li, Comparison of chemical stability and corrosion resistance of group IV metal oxide films formed by thermal and plasma-enhanced atomic layer deposition, (n.d.). doi:10.1038/s41598-019-47049-z.

[42] D. Zhang, Z. Qi, B. Wei, Z. Wang, Mater. Lett. 190 (2017) 181–184, doi:10.1016/j.matlet.2017.01.009.

[43] L. Staišiūnas, K. Leinartas, E. Juzeliūnas, D. Bučinskienė, A. Grigucevičienė, P. Kalinauskas, A. Selskis, S. Stanionytė, Surf. Coatings Technol. 397 (2020) 126046, doi:10.1016/j.surfcoat.2020.126046.

[44] T. Kokubo, H. Takadama, Biomaterials 27 (2006) 2907–2915, doi:10.1016/J.BIOMATERIALS.2006.01.017.

[45] G. Song, A. Atrens, D. StJohn, in: Magnes. Technol. 2001, John Wiley & Sons, Inc., Hoboken, NJ, USA, 2013, pp. 254–262, doi:10.1002/9781118805497.ch44.

[46] ISO 10993-12:2012 - Biological evaluation of medical devices – Part 12: sample preparation and reference materials, (n.d.). https://www.iso.org/standard/53468.html (accessed December 26, 2018).

[47] ISO 10993-5:2009 - Biological evaluation of medical devices – Part 5: tests for in vitro cytotoxicity, (n.d.). https://www.iso.org/standard/36406.html (accessed December 26, 2018).

[48] S. Nezar, N. Saoula, S. Sali, M. Faiz, M. Mekki, N.A. Laoufi, N. Tabet, Appl. Surf. Sci. 395 (2017) 172–179, doi:10.1016/j.apsusc.2016.08.125.

[49] J.H. Kim, S. Lee, H.S. Im, Appl. Surf. Sci. 151 (1999) 6–16, doi:10.1016/S0169-4332(99)00269-X.

[50] J. Yu, X. Zhao, J. Du, W. Chen, J. Sol-Gel Sci. Technol. 17 (2000) 163–171, doi:10.1023/A:1008703719929.

[51] A.R. Chourasia, J.L. Hickman, R.L. Miller, G.A. Nixon, M.A. Seabolt, Int. J. Spectrosc. 2009 (2009) 1–6, doi:10.1155/2009/439065.

[52] H. Hernández-Arriaga, E. López-Luna, E. Martínez-Guerra, M.M. Turrubiartes, A.G. Rodríguez, M.A. Vidal, J. Appl. Phys. (2017) 121, doi:10.1063/1.4975676.
[53] C. Morant, L. Galán, J.M. Sanz, Surf. Interface Anal. 16 (1990) 304–308, doi:10.1002/sia.740160163.
[54] T.S. Lim, H.S. Ryu, S.H. Hong, Corros. Sci. 62 (2012) 104–111, doi:10.1016/j.corsci.2012.04.043.
[55] G. Song, A. Atrens, D. St. John, X. Wu, J. Nairn, Corros. Sci. 39 (1997) 1981–2004, doi:10.1016/S0010-938X(97)00090-5.
[56] Q. Yang, W. Yuan, X. Liu, Y. Zheng, Z. Cui, X. Yang, H. Pan, S. Wu, Acta Biomater 58 (2017) 515–526, doi:10.1016/j.actbio.2017.06.015.
[57] Y. Liu, Z. Yu, S. Zhou, L. Wu, Appl. Surf. Sci. 252 (2006) 3818–3827, doi:10.1016/j.apsusc.2005.05.072.
[58] J. Zhao, X. Xie, C. Zhang, Corros. Sci. 114 (2017) 146–155, doi:10.1016/j.corsci.2016.11.007.
[59] M. Esmaily, J.E. Svensson, S. Fajardo, N. Birbilis, G.S. Frankel, S. Virtanen, R. Arrabal, S. Thomas, L.G. Johansson, Prog. Mater. Sci. 89 (2017) 92–193, doi:10.1016/J.PMATSCI.2017.04.011.
[60] H. Yang, K. Xia, T. Wang, J. Niu, Y. Song, Z. Xiong, K. Zheng, S. Wei, W. Lu, J. Alloys Compd. 672 (2016) 366–373, doi:10.1016/J.JALLCOM.2016.02.156.
[61] Z. Zhen, X. Liu, T. Huang, T. Xi, Y. Zheng, Mater. Sci. Eng. C. 46 (2015) 202–206, doi:10.1016/j.msec.2014.08.038.
[62] Q. Yang, W. Yuan, X. Liu, Y. Zheng, Z. Cui, X. Yang, H. Pan, S. Wu, Acta Biomater 58 (2017) 515–526, doi:10.1016/J.ACTBIO.2017.06.015.
[63] X. Li, X. Liu, S. Wu, K.W.K. Yeung, Y. Zheng, P.K. Chu, Acta Biomater 45 (2016) 2–30, doi:10.1016/J.ACTBIO.2016.09.005.
[64] A.S. Hamdy Makhlouf, in: Intell. Coatings Corros. Control, Elsevier Inc., 2015, pp. 537–555, doi:10.1016/B978-0-12-411467-8.00015-5.
[65] S. Il Pyun, Y.G. Yoon, E. Lugscheider, R. Mathesius, Surf. Coatings Technol. 61 (1993) 233–237, doi:10.1016/0257-8972(93)90231-C.
[66] C. (Christoph) Leyens, M. (Manfred) PetersJohn Wiley & Sons., Wiley InterScience (Online service), Titanium and titanium alloys : fundamentals and applications, Wiley-VCH, 2003.
[67] H. Yang, L. Huang, M. Zh, Magnes. Alloy. - Des. Process. Prop., InTech, 2011, doi:10.5772/13778.
[68] H. Hayashi, T. Saitou, N. Maruyama, H. Inaba, K. Kawamura, M. Mori, Solid State Ionics 176 (2005) 613–619, doi:10.1016/j.ssi.2004.08.021.
[69] D.R. Hummer, P.J. Heaney, J.E. Post, Powder Diffr 22 (2007) 352–357, doi:10.1154/1.2790965.
[70] R.P. Haggerty, P. Sarin, Z.D. Apostolov, P.E. Driemeyer, W.M. Kriven, J. Am. Ceram. Soc. 97 (2014) 2213–2222, doi:10.1111/jace.12975.
[71] B. Elsener, A. Rota, H. Böhni, Mater. Sci. Forum. 44–45 (1991) 29–38 https://doi.org/10.4028/www.scientific.net/msf.44-45.29.
[72] W. Li, D.Y. Li, Acta Mater 54 (2006) 445–452, doi:10.1016/j.actamat.2005.09.017.
[73] M.A. Turchanin, P.G. Agraval, Powder Metall. Met. Ceram. 47 (2008) 26–39, doi:10.1007/s11106-008-0006-3.
[74] M.L. González-Martín, L. Labajos-Broncano, B. Jańczuk, J.M. Bruque, J. Mater. Sci. 34 (1999) 5923–5926, doi:10.1023/A:1004767914895.
[75] F. Zhang, B.W. Robinson, H. De Villiers-Lovelock, R.J.K. Wood, S.C. Wang, J. Mater. Chem. A. 3 (2015) 13864–13873, doi:10.1039/c5ta02130h.
[76] A. Wiatrowski, A. Obstarczyk, M. Mazur, D. Kaczmarek, D. Wojcieszak, Characterization of HfO2 optical coatings deposited by MF magnetron sputtering, Coatings. 9 (2019). doi:10.3390/COATINGS9020106.
[77] H. Li, Q. Cui, B. Feng, J. Wang, X. Lu, J. Weng, Appl. Surf. Sci. 284 (2013) 179–183, doi:10.1016/j.apsusc.2013.07.076.
[78] T. Sun, M. Wang, Appl. Surf. Sci. 255 (2008) 396–400, doi:10.1016/j.apsusc.2008.06.123.